International Journal of Fracture **56**: 1–24, 1992.

A three-dimensional numerical investigation of fracture initiation by ductile failure mechanisms in a 4340 steel

R. NARASIMHAN[1], A.J. ROSAKIS and B. MORAN[2]
Graduate Aeronautical Laboratories, California Institute of Technology, Pasadena, California 91125, USA
[1] *Current affiliation: Indian Institute of Science, Bangalore, India*
[2] *Current affiliation: Northwestern University, Evanston, Illinois 60208, USA*

Received 20 November 1989; accepted in revised form 30 May 1991

Abstract. Fracture initiation in ductile metal plates occurs due to substantial tunneling of the crack in the interior of the specimen followed by final failure of side ligaments by shear lip formation. The tunneled region is characterized by a flat, fibrous fracture surface. This phenomenon is clearly exhibited in a recent experimental investigation [8] performed on pre-notched plates of a ductile heat treatment of 4340 carbon steel. Experimental evidence obtained in [8] suggests that tunneling begins at an average value of J which is significantly lower than the J value at which gross initiation is observed on the free surface. In the present work, fracture initiation in the 4340 steel specimens used in [8] is analyzed by performing a 3-dimensional numerical simulation. A damage accumulation model that accounts for the ductile failure mechanisms of void nucleation, growth, and void coalescence is employed. Results indicate that incipient Cmaterial failure at the center-plane of the 3-dimensional specimen is predicted quite accurately by this computation. Also, good agreement between results obtained at the center-plane of the 3-dimensional specimen and a plane strain analysis, suggests that a local definition of J can be used to characterize fracture initiation in the center-plane of the specimen. Finally, radial and thickness variations of the stress and porosity fields are examined with the view of understanding the subsequent propagation of the failure zone.

1. Introduction

The most important micro-mechanical processes that are operative during ductile fracture are void nucleation, growth and coalescence. This is evidenced by the many depressions or dimples that are often observed on the fracture surface of a ductile material. Void nucleation occurs due to brittle cracking or interfacial decohesion of inclusions. These inclusions could be second-phase particles added intentionally to the matrix to cultivate specific properties such as increased yield strength or other particles such as slags or impurities which serve no positive function. It has been observed that void nucleation in AISI 4340 steel occurs first at lower strains from large inclusions such as sulfide particles [1]. This is followed by growth of voids which also takes place more rapidly around larger inclusions in the matrix. While void nucleation itself could be relatively independent of the level of tensile stress triaxiality (see [1]), experimental and theoretical studies [1–3] clearly demonstrate that void growth rates are increased substantially by increasing the level of triaxial tension.

The final process that completes the ductile fracture phenomenon is void coalescence which would occur either due to necking down of ligaments connecting large voids [2] or due to a **void-sheet** formation [1, 4, 5]. This is the result of an intense deformation band which begins to concentrate along the ligaments connecting neighboring voids after they have grown to a critical size in relation to their spacing [1, 6, 7]. This is followed by the nucleation of voids at smaller particles such as cementile particles [1] which leads to the formation of microcracks that connect the large voids.

In a recent work, Zehnder and Rosakis [8] studied fracture initiation in three-point bend specimens of a 4340 carbon steel using optical experimental measurements. Their work was complemented by a 3-dimensional finite element simulation by Narasimhan and Rosakis [9] using a small strain, incremental J_2 flow theory of plasticity. The specimens employed in the experiments of [8] were 10 mm thick. A photograph of the fracture surface obtained from one of the specimens used in this work is displayed in Fig. 1. This specimen was loaded to just below the fracture initiation point. It was then embrittled by cooling down to liquid nitrogen temperature and broken open in a dropweight tower.

Two distinct features may be observed on the fracture surface of Fig. 1. The first one involves a central, fibrous, **flat-fracture** zone which has the shape of a thumb-nail and is about 6 mm in length. The second one pertains to inclined failure surfaces, usually referred to as **shear-lips**, adjacent to the free surfaces of the specimen. The flat-fracture region is characterized by the ductile failure mechanisms of void nucleation and growth described above. The tensile stress triaxiality is very high near the crack front at the center-plane of the specimen as compared to its free-surfaces (see, for example, the numerical results in [9]). This results in rapid growth and coalescence of voids near the crack front adjacent to the center-plane of the specimen leading ultimately to the formation of a 'damage zone' or 'tunneled region'.

The tunneled region adjoining the center-plane progressively spreads forward and also sideways with increasing load. The load is then transferred to the side-ligaments (portion of the crack front between the tunneled core and the free surface). A stage is finally reached during which excessive softening of the material in the damage zone, coupled with the highly non-uniform stress state prevailing along the crack front, triggers the shear failure of the side ligaments through the formation of shear-lips. The shear-lips are intense strain concentration

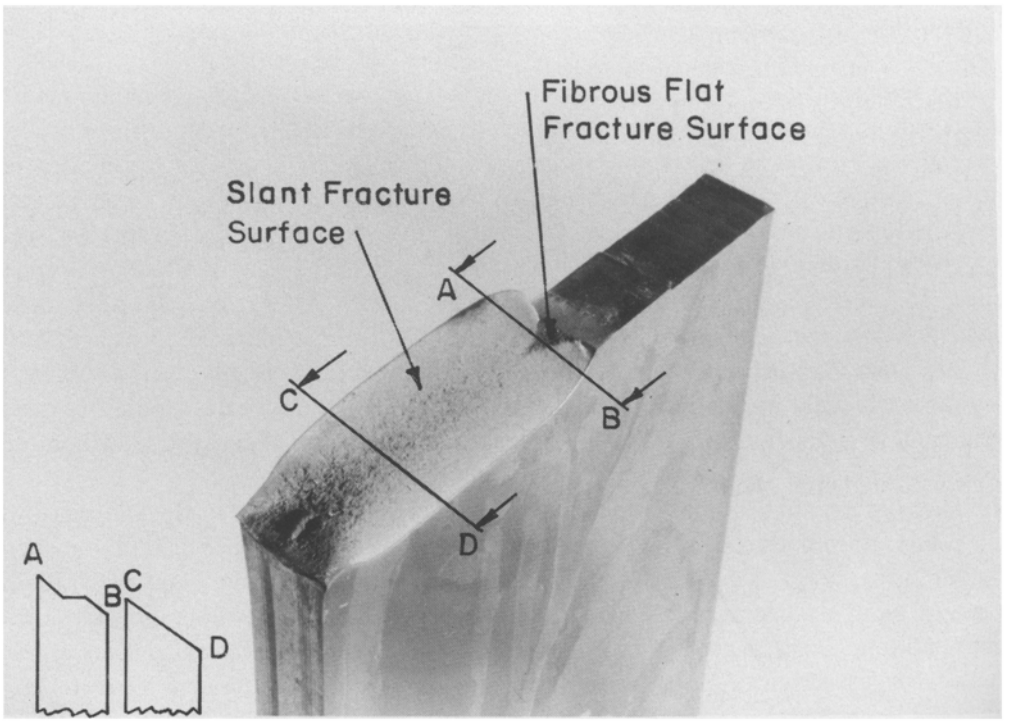

Fig. 1. Photograph of fracture surface of 4340 steel specimen used in [8].

bands that are inclined at approximately 45° to the free surface. It is at this point that fracture initiation is first observed on the free surface. In the experiments described in [8], gross initiation on the free surface was observed corresponding to a J value of 420 KN/m. On the other hand, evidence based on strain gauge and optical measurements from the vicinity of the crack tip [8, 10] suggests that tunneling occurs at $J = 200 - 250$ KN/m.

The purpose of the present investigation is to simulate the static loading of the three-point bend specimen employed in [8] using three-dimensional finite elements with the view of studying the initiation and subsequent development of crack tunneling. The essential difference between the present investigation and [9] is that a damage accumulation model [11, 12] that accounts for void nucleation, growth, and final material failure by void coalescence has been employed in the present computations. This may be viewed as an equivalent continuum mechanics approach as opposed to a direct study of the deformation behaviour of individual voids [2, 3]. The material model used here has a failure criterion incorporated in it which causes the material stress carrying capacity to vanish locally near a point when the volume fraction of voids reaches a critical value [12]. The details pertaining to the material model are outlined in Section 2.

The results of [9] suggest that plane strain conditions prevail near the crack tip of the specimen. In order to understand how accurately a two-dimensional plane strain analysis predicts **local material failure** in the center-plane of the three-dimensional specimen, a plane strain calculation has also been performed using the same in-plane mesh geometry used in the three-dimensional calculations (see Section 3). One of the important issues under investigation here (see Section 4) is the evolution of volume fraction of voids near the tip up to the point of incipient material failure. Another issue under study is the radial and thickness variations of the macroscopic stress and void volume fraction so that the subsequent propagation of the damage zone could be understood. While it was possible to simulate the actual propagation of the damage zone for the simpler plane strain case, the three-dimensional computations could not be continued much beyond the fracture initiation point because of some numerical difficulties (see Section 4).

Several investigators have used the damage accumulation model due to Gurson [11] to study ductile failure under various situations. Some of this literature that is relevant to the present work is reviewed below. Needleman and Tvergaard [11] analyzed cup-cone fracture in a round tensile bar. In their work, they were able to simulate both the formation of a damage zone at the center of the necked region of the bar and its subsequent propagation towards the free surface. Aoki et al. [13] and Aravas and McMeeking [14] examined the interaction between a crack tip and a void. The presence of small-scale voids is accounted for in studies by using the Gurson model [11]. Jagota et al. [15] conducted a finite element study of the stress and porosity fields near a plane strain stationary crack under mode-I, small-scale yielding conditions. They investigated fracture by slip-induced cleavage as well as by a void coalescence mechanism with the view of predicting the fracture toughness.

In a very recent work, Becker et al. [16] analyzed ductile failure in Al-Li alloys due to crack growth along grain boundaries by nucleation and growth of micro-voids. They found that calculated values of K_{Ic} and tearing modulus from their numerical simulation were in reasonable agreement with experimental results. Becker et al. [17] have studied void growth and ductile failure in notched bars both numerically and experimentally. The influence of material rate sensitivity and void nucleation and growth on fracture initiation in a circumferentially notched bar was examined by Moran et al. [33].

2. Constitutive model

The material constitutive model employed in this work is the one proposed by Gurson [11] which is a continuum elastic-plastic model that accounts for void nucleation and growth. Gurson [11] proposed his constitutive equations based on an approximate analysis of a rigid plastic solid containing a spherical cavity. This model was subsequently modified by Tvergaard and Needleman [12], since in its original form the complete loss of material stress carrying capacity due to void coalescence was not predicted at a realistic value of void volume fraction. The essential features of the material model are outlined below within the context of a small-strain incremental plasticity theory. A more elaborate discussion may be found in [12, 14].

The modified Gurson yield function Φ which depends upon the macroscopic (average, aggregate) stress $\boldsymbol{\sigma}$, the microscopic (matrix) tensile flow stress σ_m and the current void volume fraction f is given by

$$\Phi(\boldsymbol{\sigma}, \sigma_m, f) = \frac{\sigma_e^2}{\sigma_m^2} + 2f^* q_1 \cosh\left\{\frac{\sigma_{kk}}{2\sigma_m}\right\} - \{1 - (q_1 f^*)^2\} = 0 \tag{2.1}$$

It should be noted that the above yield function depends both on the stress deviator S_{ij} through the macroscopic equivalent stress $\sigma_e = (\frac{3}{2} S_{ij} S_{ij})^{1/2}$, and also on the hydrostatic stress $\sigma_{kk} = tr\boldsymbol{\sigma}$. Tvergaard [5] introduced the additional parameter q_1, with a value of 1.5 to obtain better agreement with numerical studies of periodically distributed cylindrical or spherical voids. The modification of the yield condition to account for final material failure by void coalescence is achieved through the function $f^*(f)$ which is defined as [12]:

$$f^* = \begin{cases} f & \text{for } f \leqslant f_c \\ f_c + K(f - f_c) & \text{for } f > f_c. \end{cases} \tag{2.2}$$

The parameter f_c in the above equation represents the void volume fraction at which void coalescence is **first** observed. Also, K in (2.2) is a constant which will be defined below. Equation (2.2) implies that the original Gurson model is applied to describe the material behaviour as long as $f \leqslant f_c$, while an **accelerated** void evolution law is introduced for $f > f_c$ leading to rapid loss of material stress carrying capacity.

It can be observed from the yield condition (2.1) that the material stress carrying capacity vanishes when $f^* = f_u^* = 1/q_1$. Now if experiments or analysis indicate that the void volume fraction at final failure is f_F then K is given by:

$$K = \frac{f_u^* - f_c}{f_F - f_c}. \tag{2.3}$$

Experimental studies [1, 6, 7] indicate that the ligament connecting two neighboring voids fails by shear band formation or by simple necking when the size of voids has grown to the order of magnitude of their spacing. An estimate of f_c obtained in [7] from a simple model is 0.15. Also, a numerical investigation by Andersson [18] suggests that $f \simeq 0.25$ at final failure. Based on the above studies, f_c and f_F are chosen as 0.15 and 0.25, respectively. Further justification for the choice of $f_F = 0.25$ for AISI 4340 carbon steel is found in Appendix A.

A matrix effective plastic strain ε_m^P is assumed to be related to the matrix tensile flow stress σ_m by a uniaxial equation of the form,

$$\dot{\varepsilon}_m^P = \left(\frac{1}{E_t} - \frac{1}{E}\right)\dot{\sigma}_m. \tag{2.4}$$

Here a superimposed dot implies a material time derivative and E_t and E are the current tangent modulus and Young's modulus of the matrix material. An equivalent plastic work expression,

$$\sigma_{ij}\dot{\varepsilon}_{ij}^P = (1 - f)\sigma_m\dot{\varepsilon}_m^P, \tag{2.5}$$

completes the evolution law for σ_m. The void volume fraction f is allowed to evolve both due to growth of existing voids and nucleation of new voids, so that,

$$\dot{f} = \dot{f}_{\text{growth}} + \dot{f}_{\text{nucleation}}. \tag{2.6}$$

The growth law which is described by,

$$\dot{f}_{\text{growth}} = (1 - f)\dot{\varepsilon}_{kk}^P, \tag{2.7}$$

is an outcome of the plastic incompressibility of the matrix material. It should, however, be noted that the **macroscopic** material response does not satisfy plastic incompressibility due to the existence of voids.

In the present work, a plastic strain controlled void nucleation law is assumed from the form [12],

$$\dot{f}_{\text{nucleation}} = A\dot{\varepsilon}_m^P, \tag{2.8}$$

where $A(\cdot)$ is a function of the equivalent matrix plastic strain ε_m^P. The function A is chosen as [19]:

$$A = \frac{f_n}{s_n\sqrt{2\pi}}\exp\left[-\frac{1}{2}\left(\frac{\varepsilon_m^P - \varepsilon_n}{s_n}\right)^2\right], \tag{2.9}$$

so that void nucleation follows a normal distribution about a mean nucleating strain ε_n and with a standard deviation s_n. In the above equation, f_n denotes the volume fraction of void nucleating particles. The values of f_n, s_n and ε_n were chosen as 0.04, 0.1 and 0.3 respectively. These values were chosen in such a way, so that the nucleation of voids as predicted by (2.8) and (2.9) was in reasonable agreement with the microstructural observations of Cox and Low [1] for AISI 4340 steel. (See Appendix A for comparison with the micromechanical observation of [1].)

The flow rule is assumed to obey macroscopic normality, so that,

$$\dot{\varepsilon}_{ij}^P = \dot{\lambda}\frac{\partial\Phi}{\partial\sigma_{ij}}. \tag{2.10}$$

As pointed out by Berg [20], macroscopic normality follows from the fact that the matrix material exhibits normality. In the above equation, the plastic parameter $\dot{\lambda}$ is non-negative since plastic work rate $\sigma_{ij}\dot{\varepsilon}^P_{ij} \geqslant 0$. The loading/unloading conditions may then be expressed as follows:

$$\Phi(\boldsymbol{\sigma}, \sigma_m, f) \leqslant 0 \tag{2.11a}$$

$$\dot{\lambda} \geqslant 0 \tag{2.11b}$$

$$\Phi\dot{\lambda} = 0. \tag{2.11c}$$

Equation (2.11a) requires the stress state to be confined to on or inside the yield surface. Along any process of loading, conditions (2.11) must hold simultaneously. For $\Phi < 0$, (2.11c) necessitates $\dot{\lambda} = 0$ so that elastic material behaviour is obtained. On the other hand, plastic flow is characterized by $\dot{\lambda} > 0$, which in view of (2.11c), requires the satisfaction of the yield condition $\Phi = 0$.

The total strain rate is taken to be the sum of the elastic and plastic parts, $\dot{\varepsilon}_{ij} = \dot{\varepsilon}^e_{ij} + \dot{\varepsilon}^P_{ij}$, where,

$$\dot{\varepsilon}^e_{ij} = C_{ijkl}\dot{\sigma}_{kl}. \tag{2.12}$$

Here C_{ijkl} are the Cartesian components of the constant, isotropic, positive definite elasticity four tensor.

3. Numerical procedure

The three-point bend specimen shown in Fig. 2a was modelled using three-dimensional finite elements. The geometry of the in-plane mesh is shown in Fig. 2b. Due to symmetry, only a quarter of the specimen was simulated with appropriate boundary conditions imposed on the planes of symmetry. The mesh consists of 6 layers of elements (through the half thickness of the plate). Each layer is composed of 320 eight-noded brick elements. The layer interfaces are located at $x_3/h = 0$, 0.113, 0.226, 0.339, 0.415, 0.469, and 0.5. It should be noted that the layers become thinner as the free surface is approached in order to model the corner singularity. A detailed in-plane region near the notch tip is displayed in Fig. 2c. The initial notch diameter b_0 is chosen as $h/50$, where h is the plate thickness ($h = 1$ cm). The in-plane dimension of the smallest element near the notch tip is $b_0/8$ (which is equal to $h/400$). Two-dimensional plane strain calculations were performed with the same in-plane mesh (Fig. 2b).

The size of b_0 in the numerical calculation is dictated by the dimensions of the initial notch in the experiments described in [8].

The response of the matrix material in uniaxial tension was characterized by a piece-wise power hardening law of the form:

$$\frac{\varepsilon_m}{\varepsilon_0} = \begin{cases} \sigma_m/\sigma_0 & \sigma_m \leqslant \sigma_0 \\ (\sigma_m/\sigma_0)^n & \sigma_m > \sigma_0 \end{cases}$$

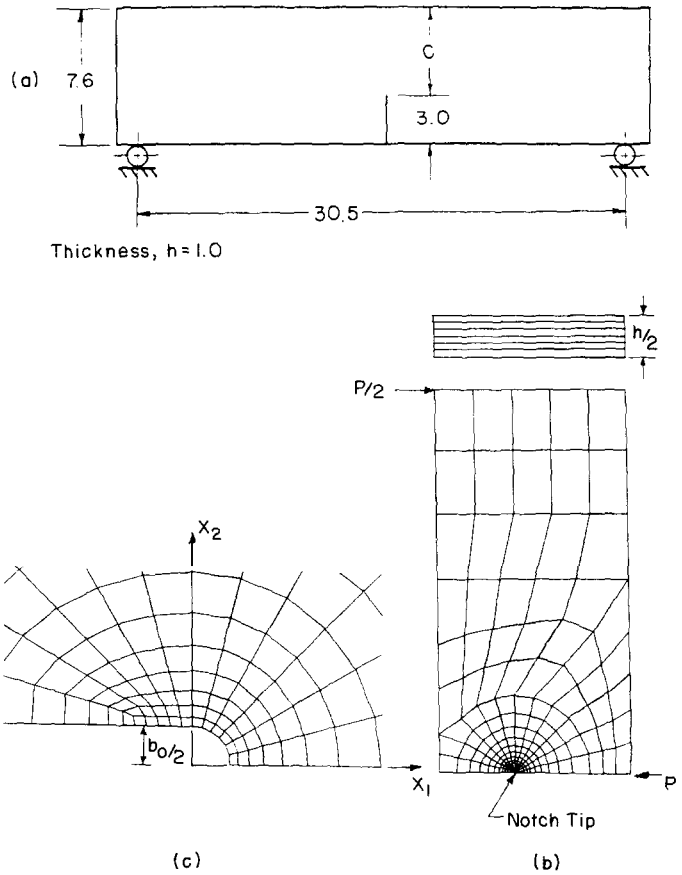

Fig. 2. (a) Test specimen geometry. All dimensions are in cm. (b) Mesh used in finite element analysis. (c) Details of in-plane mesh near the notch tip.

with a hardening exponent $n = 22$ and yield stress $\sigma_0 = 1030$ Mpa. These values were also chosen in the previous investigation [9] to match the macroscopic constitutive properties of the particular heat treatment of 4340 carbon steel used in the experiments [8].

The governing finite element equilibrium equations were derived from a small-strain virtual work principle (see [21]). These non-linear equations were solved incrementally using a quasi-Newton method (BFGS) [22]. The stress computations were performed using an explicit algorithm with subincrementation (see [21] and also Appendix B).

As noted in Section 2, complete loss of material stress carrying capacity occurs when $f^* = f_u^* = 1/q_1$ (or equivalently when $f = f_F$), resulting in local failure. This implies that the material separates completely at this point and a traction free surface develops. This failure criterion was implemented in the present computations following the method suggested in [23, 14]. In this method, the matrix yield strength σ_m and void volume fraction f, which evolve according to the laws described in Section 2, are held constant after f reaches a value of $0.95 f_F$. In other words, subsequent evolution of σ_m and f are frozen. The macroscopic material response is then elastic-perfectly plastic with a small pressure dependent yield stress. As pointed out in [14], the condition $f = 0.95 f_F$ was used instead of $f = f_F$ because as f approaches f_F, the macroscopic equivalent stress σ_e approaches zero, causing numerical difficulties. An alternative element vanishing technique has been proposed by Tvergaard [23] to model the failure criterion.

4. Results and discussion

4.1. Variation of void volume fraction and notch opening with J

The J integral for a three-dimensional crack front is defined over a cylindrical surface surrounding the crack front (see [24]). This surface integral may also be interpreted as the energy released due to unit (normal) virtual crack extension along the entire crack front. An **average** value, denoted here by J, can then be obtained by dividing the above quantity by the length of the crack front [25]. A local energy release rate has also been defined in the literature (see, for example, [25–27]) as a pointwise measure along the crack front. It has been suggested that this local definition of energy release rate [26, 27], denoted here by $\hat{J}(x_3)$, plays a role as a characterizing parameter of the crack tip fields. This suggestion has been motivated by the assumption that plane strain conditions prevail through the thickness as the crack front is approached. This issue was investigated in the previous work [9] by the authors on three-dimensional effects near the crack front on a three-point bend specimen. There is strong evidence from this study [9] that the plane strain HRR field [28, 29] dominates close to the crack front in the interior (near the center-plane) of the specimen. This provides support for the use of local $\hat{J}$ value to characterize crack initiation at the center-plane of the specimen.

The domain integral method proposed in [25–27] has been used to compute J and $\hat{J}$. The variation of $\hat{J}$ (normalized by the average value of J) versus normalized distance x_3/h along the crack front is shown in Fig. 3 for different levels of applied load P. This figure displays a considerable variation of $\hat{J}$ through the thickness with increasing plastic deformation and is similar to earlier published results based on J_2 flow theory of plasticity (see [9, 25]). It should be

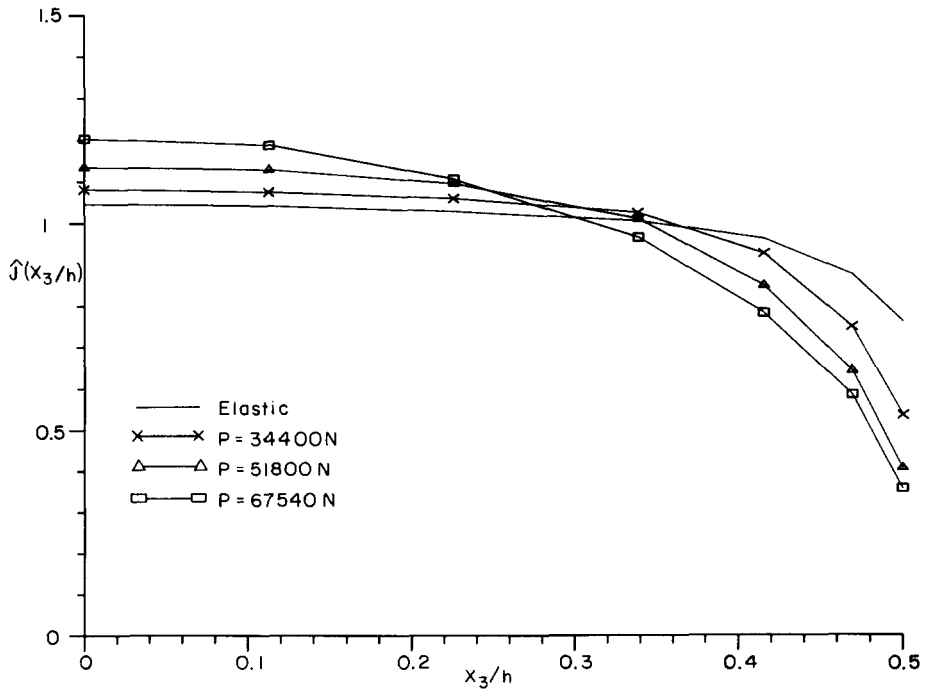

Fig. 3. Variation of $\hat{J}$ through the thickness for different loads.

noted that the value of $\hat{J}$ at the center-plane ($x_3/h = 0$) is much higher than that at the free surface ($x_3/h = 0.5$) for large load levels.

The issue pertaining to the use of $\hat{J}$ as a local fracture parameter to predict crack initiation near the center-plane of the specimen is examined further in the present work. In Fig. 4, the evolution of void volume fraction f with local J value is shown for the element nearest to the three dimensional notch front that failed first. For the plane strain case, the element immediately ahead of the notch tip, which is denoted by B in the inset diagram given in Fig. 4, was the first to fail. The variation of f versus J in this element is represented by the dashed line. In the 3-D simulation, the element corresponding to A (see the insert diagram) adjacent to the center-plane of the specimen exhibited incipient material failure. The f versus $\hat{J}$ relationship for this element is displayed by the solid line in the figure. It should be noted that the evolution of void volume fraction (with respect to local J) at the center-plane of the 3-D specimen is remarkably close to plane strain up to the point of incipient material falure. The $\hat{J}$ value corresponding to the center-plane at which incipient damage occurs is around 250 KN/m and is very close to the value of 270 KN/m predicted by the plane strain calculation. It can be deduced from Fig. 3 that this corresponds to an **average** J value of about 200–250 KN/m. This average value is of relevance when comparison with the results of experiments is desired, since experimental techniques such as the optical technique described in [8] can only provide the average value of J. Indeed, the measured value of J average reported in [8] at the **onset of tunneling** lies within the predicted range. Hence, the present damage model calculation appears to predict the onset of crack tunneling in the center-plane of the specimen quite accurately.

The notch opening ($b - b_0$), normalized by the initial notch diameter b_0, is plotted against $\hat{J}/(\sigma_0 b_0)$ in Fig. 5. Results are once again represented corresponding to plane strain and the

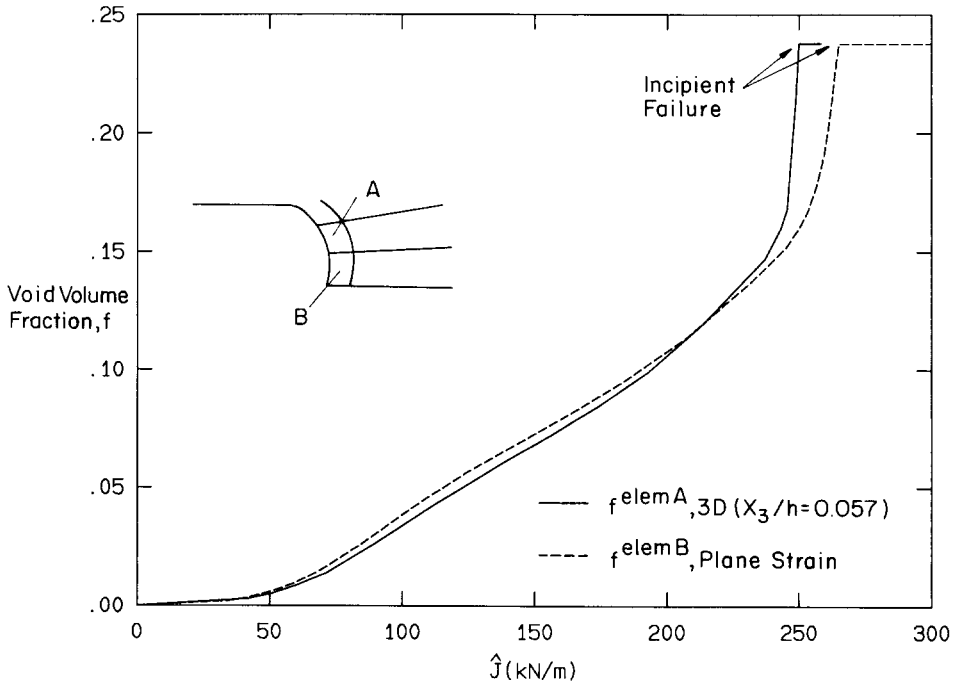

Fig. 4. Evolution of void volume fraction vs. $\hat{J}$ in the element near the notch tip that was first to fail. Comparison between plane strain and 3-D center-plane results.

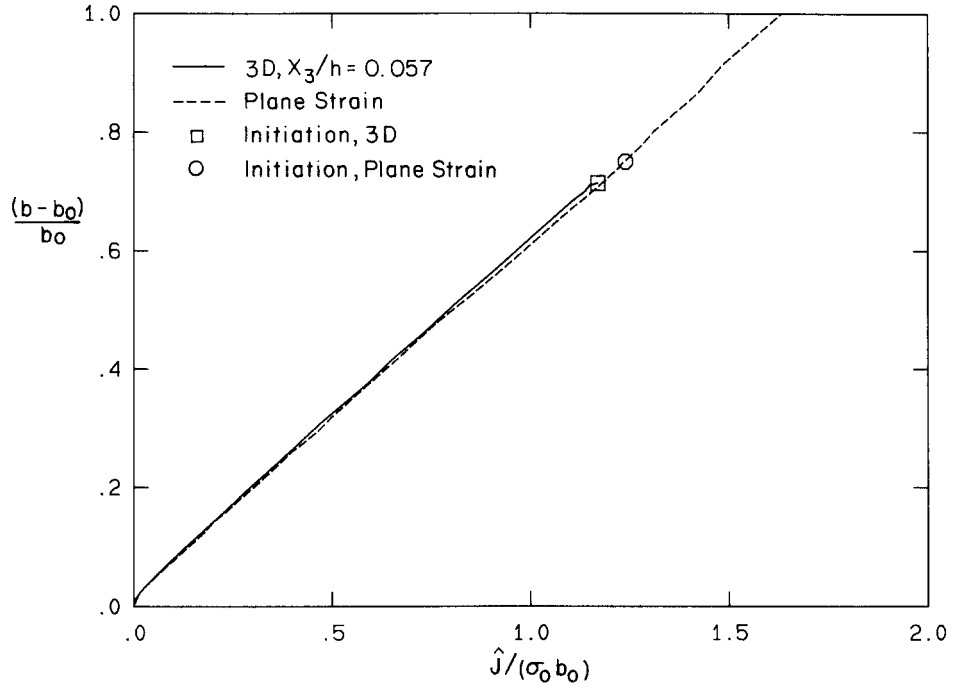

Fig. 5. Variation of normalized notch opening vs. $\hat{J}/(\sigma_0 b_0)$. Comparison between plane strain and 3-D center plane results.

center-plane of the 3-D specimen. The current notch diameter b was calculated from the numerical solutions using the 45° intercept procedure [30]. It can be seen that the 3-D center-plane result agrees very well with plane strain and displays an almost linear relationship between the notch opening and the local J value.

From Fig. 5, it can be deduced that $b - b_0 \simeq 0.6\hat{J}/\sigma_0$ in the center-plane of the 3-D specimen. This is in very good agreement with previous published results based on the J_2 flow theory for low hardening materials under plane strain. In the earlier numerical investigation of this specimen geometry and material [9], with an initially sharp crack, a normalized crack tip opening $\delta_t/(J/\sigma_0)$ of 0.62 – 0.60 was obtained corresponding to plane strain. Shih [30] reports a value of $\delta_t/(J/\sigma_0)$ that varies from 0.65 to 0.58 for a Cracked Bend Bar of perfectly plastic material under plane strain as the extent of crack tip yielding varies from contained to fully plastic conditions.

The results of Figs. 4 and 5 discussed above corroborate the view that plane strain conditions prevail near the notch tip close to the center-plane of the 3-D specimen. They also provide justification for the use of the local $\hat{J}$ value to describe fracture initiation (or tunneling) in the center-plane of the specimen.

4.2. Contour plots near the notch tip

4.2.1 Plane strain

The contours of macroscopic equivalent stress σ_e around the notch tip are shown in Fig. 6 for the plane strain case after incipient material failure (Fig. 6a) and after the failure of three elements ahead of the notch tip (Fig. 6b). The contour levels are also indicated in the figure. It is

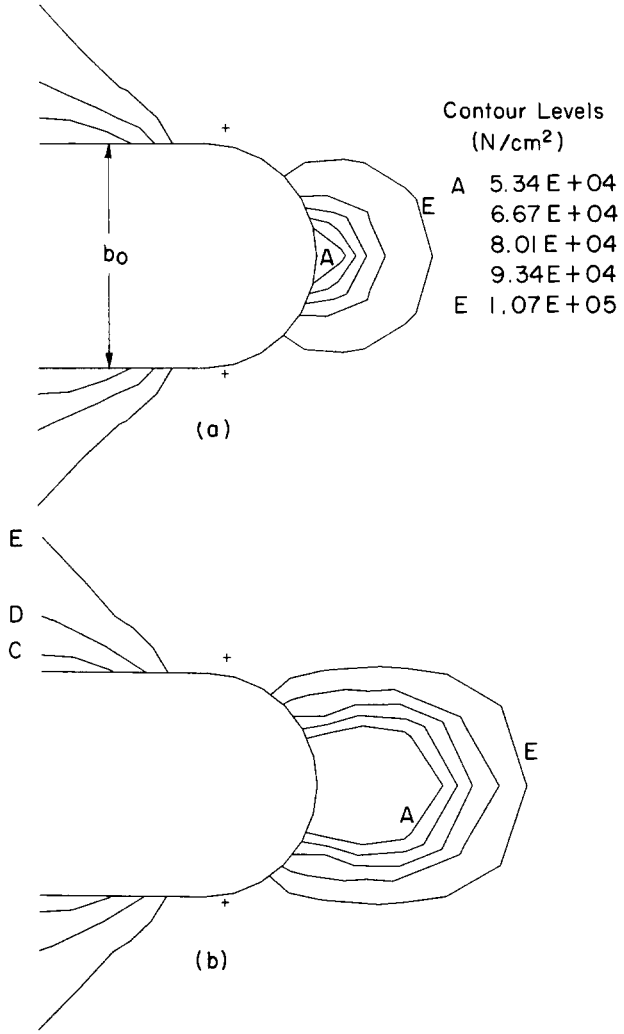

Fig. 6. Contours of macroscopic equivalent stress σ_e for plane strain: (a) after failure of the first element and (b) after failure of three elements.

recalled that the initial yield stress of the matrix material is 1.03×10^5 N/cm^2 and that the matrix material exhibits very little strain hardening ($n = 22$). It can be noticed from Fig. 6a that σ_e **decreases** as the notch tip is approached indicating that **material softening** has occurred in this region. This has eventually led to complete loss of material stress carrying capacity (refer to Section 2) and to the emergence of a damage zone. In Fig. 6b, the region over which material softening has occurred has spread forward with the failure of subsequent elements.

The contours of void volume fraction around the notch tip are presented in Fig. 7 after incipient material failure (Fig. 7a) and after the damage has spread to three elements (Fig. 7b). These figures offer more precise information on the shape and size of the damage zone which is identified by the shaded regions within the contour F. It can be noticed from Fig. 7b that the damage zone has spread directly in front of the notch tip with the failure of subsequent elements. Another observation that can be made from Fig. 7b is that the damage zone is strongly reminiscent of a sharp crack profile (see, for example, [31, 32]). The reasons for the sharp crack

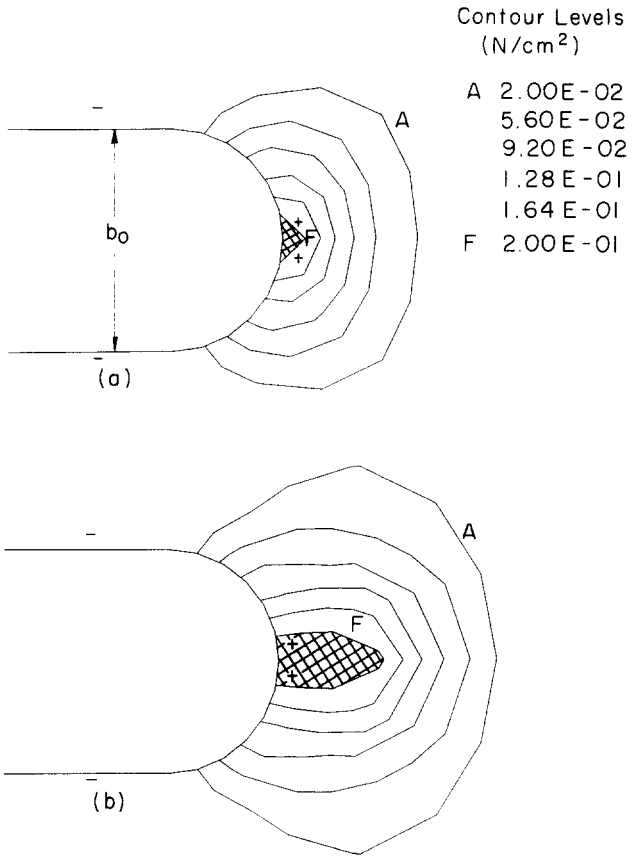

Fig. 7. Contours of void volume fraction f near the notch tip for plane strain: (a) after failure of first element and (b) after failure of three elements. The damage zone is indicated by the shaded region.

profile during crack growth in an elastic-plastic material as opposed to a blunted shape before initiation are the decreased strain singularity folds and the failure of the strain fields to re-focus at the new crack tip [32]. As emphasized by Rice [32], this decreased strain singularity is the source of stable crack growth in elastic-plastic materials.

4.2.2. Three-dimensional simulation

A three-dimensional view of the near-tip mesh is shown in Fig. 8. The top surface in the figure corresponds to the free surface of the plate and the bottom (hidden) one to the center-plane. The notch tip is located along the bright portion near the center of the semi-cylindrical region. Due to the high density of elements, this region is obscured in the figure. Figure 9 displays three-dimensional colour band contours of macroscopic equivalent stress σ_e. The range of contour levels corresponding to various colour bands is indicated in the inset diagram of the figure. The border between the bright red and bright yellow bands (corresponding to a level of $\sigma_e \simeq 1.03 \times 10^5$ N/cm^2) is an approximate indication of the plastic zone. The maximum plastic zone extent in this figure is about 0.6 h. The shape and size of the plastic zone obtained here is very close to that reported in [9] on the basis of the J_2 flow theory at around the same load level. A close-up of the notch front region is shown in Fig. 10. The color bands of σ_e clearly show a drop of σ_e very near the notch front, in the interior of the specimen. (See yellow region parallel

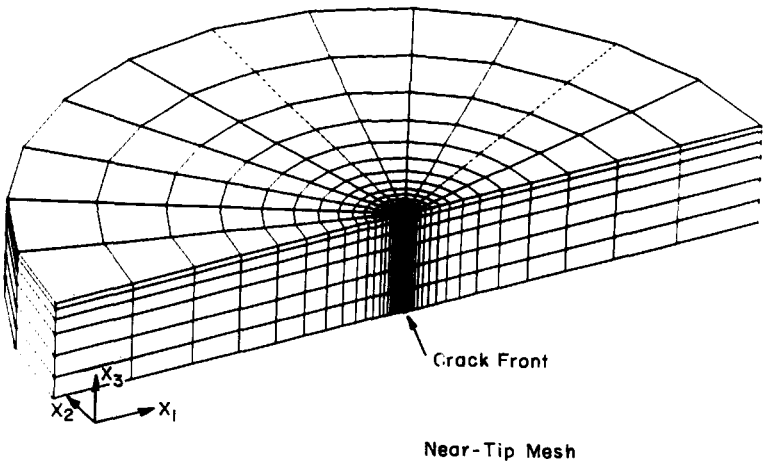

Fig. 8. A three-dimensional view of the near-tip mesh.

to the notch front.) This is due to damage accumulation near the front and the resulting collapse of the yield surface.

In Fig. 11, colour contour bands of the macroscopic hydrostatic stress $(\sigma_{11} + \sigma_{22} + \sigma_{33})/3$ through the (semi-) thickness of the plate are given. The top part of the diagram corresponds to the free surface and the bottom to the center-plane. It can be observed that there is a very strong variation of the hydrostatic stress through the thickness with the values at the center-plane being much higher than those at the free surface. The radial variation of the hydrostatic stress ahead of the notch tip corresponding to various planes through the specimen thickness will be discussed later (see Fig. 15).

In Fig. 12, line contours of macroscopic equivalent stress are displayed from a very detailed region near the notch tip at the point of incipient material failure. Results are shown for three different planes through the specimen thickness. These are near the center-plane of the specimen (Fig. 12a), near the quarter-plane (Fig. 12b), and near the free surface (Fig. 12c). The contour levels corresponding to each case are also included in the figures. It should be noted that there is considerable material softening near the center-plane close of the notch tip. The softening region is much diminished near the quarter-plane and is virtually non-existent near the free surface (see Fig. 12c).

In Fig. 13, contours of void volume fraction very near the notch tip are shown at the point of incipient material damage. As in Fig. 12, results are given for three different planes taken through the specimen thickness. The damage zone is just starting to form near the center-plane (see Fig. 13a) at the locations indicated by the shaded zones. (Symmetry about the center line of the notch has been utilised in drawing the contours below the center-line.) The contour levels of f in the quarter-plane and free surface (see Figs. 13b and c) are much lower than in the center-plane and the material damage has not yet spread to these regions.

It would be extremely interesting to follow the further development of the damage zone and compare it with the tunneled region from the experiments (see Fig. 1). However, in the present work, the computations were stopped after incipient material failure because of numerical difficulties caused by elastic unloading of some elements surrounding the damage zone. This led to lack of convergence to equilibrium in the quasi-Newton iteration algorithm mentioned in Section 3. It was possible to overcome this difficulty in the plane strain simulation by taking small load increments and by using the full-Newton iteration scheme. But the prohibitive cost of carrying out a 3-dimensional, non-linear computation precluded these alternatives for the 3-D

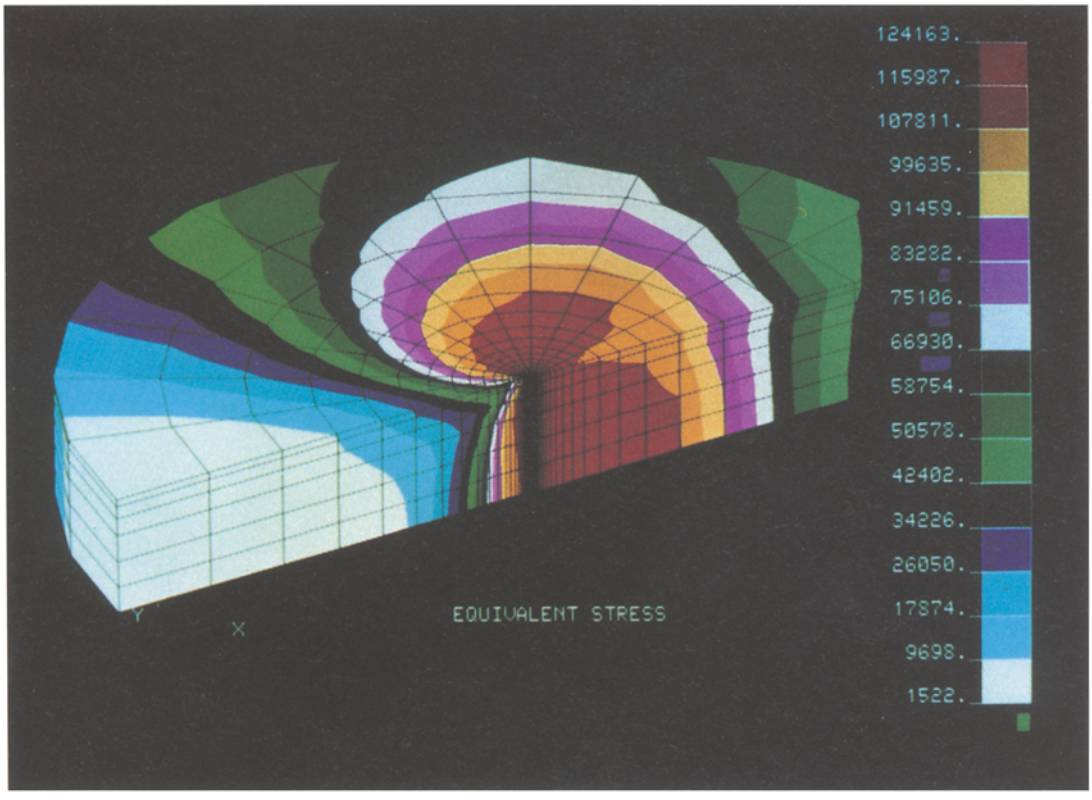

Fig. 9. Three-dimensional colour band contours of σ_e (global view).

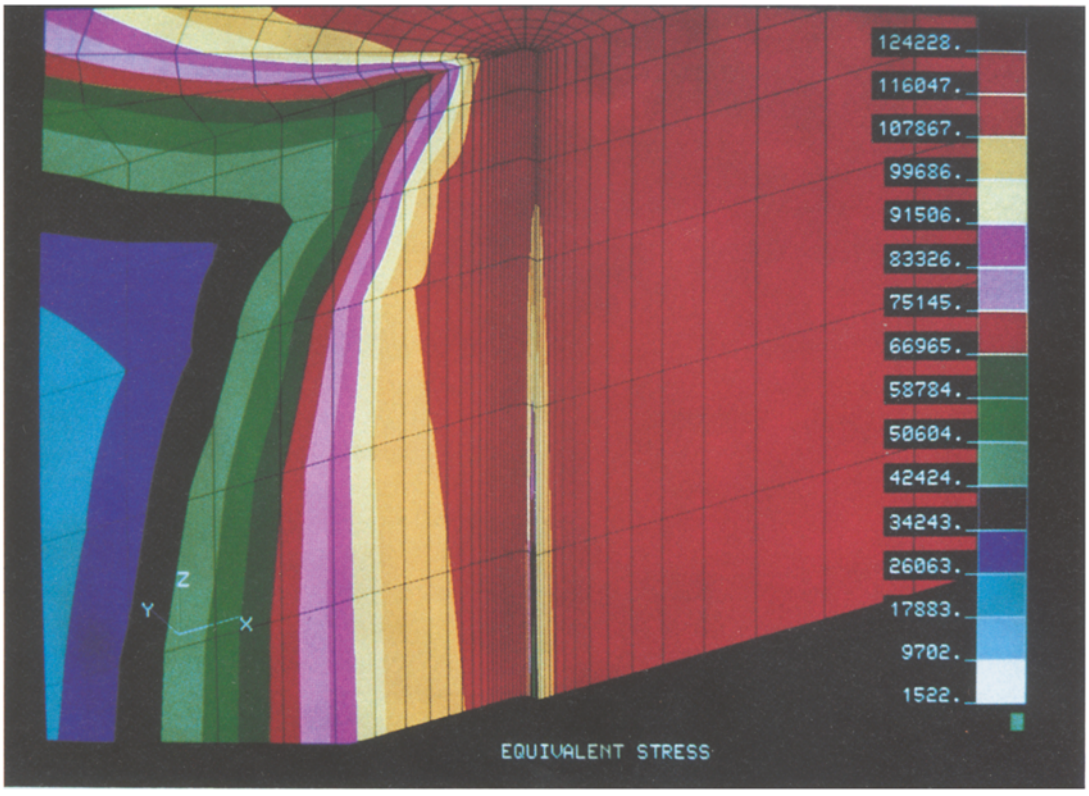

Fig. 10. Three-dimensional colour band contours of σ_e (close-up view).

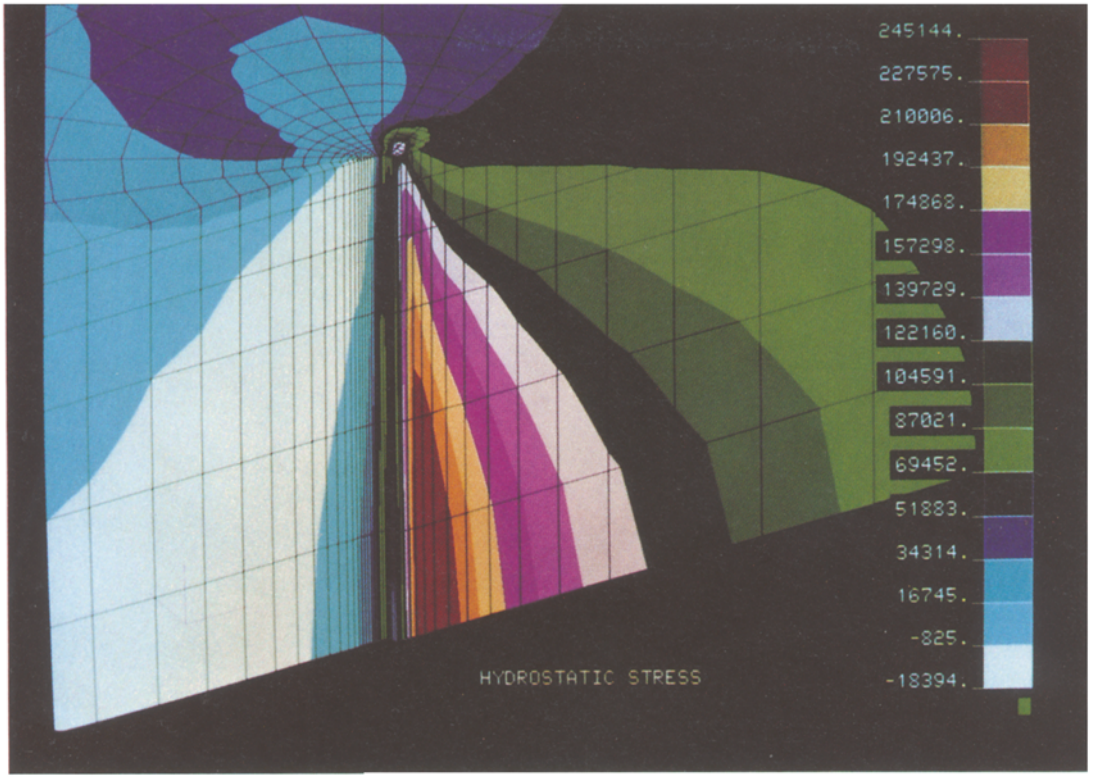

Fig. 11. Three-dimensional colour band contours of hydrostatic stress, illustrating the variation through the (semi-) thickness of the plate (close-up view).

case. In this connection, it must be mentioned that it would be advantageous to perform these computations with a rate dependent constitutive model [16, 17] which does not have an explicit loading/unloading condition.

Nevertheless, some comments may be made about the subsequent propagation of the damage zone on the basis of Fig. 13. On comparing Figs. 13a and b, it may be seen that the levels of void volume fraction at equivalent distances from the notch tip are much lower in the quarter-plane as compared with the center-plane. Hence, further failure is expected to occur near the center-plane, before the elements near the quarter-plane begin to fail. This would then result in a 'thumb-nail' shaped damage zone similar to that observed in the experiments (see Fig. 1).

Also, it is likely that with further failure of elements in the center-plane, the damage zone would link up with the symmetry line ahead of the notch tip. However, a zig-zag or wavy damage surface across the plastic region in the front of the notch is also possible. This has been suggested by Berg [20] for a material that exhibits dilational plastic straining similar to the one used in the present investigation.

Finally, it is noted that the lack of a length scale in the constitutive equations (2.1)–(2.12) may introduce a mesh-size effect into the pattern of failure propagation. The onset of failure is expected to be accurately predicted, however, and no significant mesh effects are expected for the limited amount of 'crack growth' considered in the present calculations.

4.3. Thickness and radial variations

Figure 14 illustrates the variation of the void volume fraction f through the thickness of the specimen. It must be recalled that the center-plane is located at $x_3/h = 0$ and the free-surface at

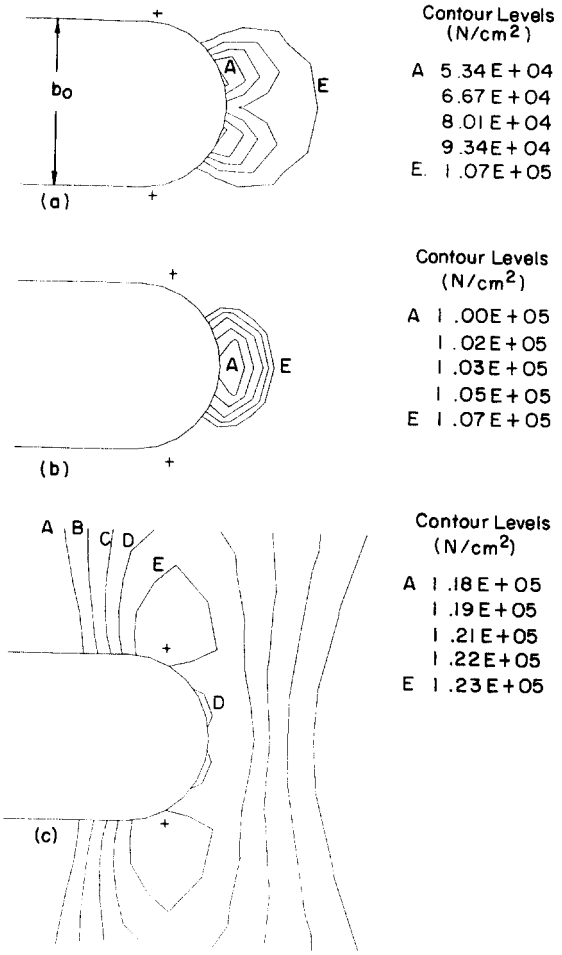

Fig. 12. Contours of σ_e in three different planes through the specimen thickness: (a) $x_3/h = 0.057$, (b) $x_3/h = 0.282$, (c) $x_3/h = 0.485$.

$x_3/h = 0.5$. Each of the curves in the figure correspond to different radial distances ahead of the notch tip as listed in the legend. A very strong variation of the void volume fraction through the thickness can be observed from this figure. For example, corresponding to the curve 'a' ($r/h = 0.001$), the void volume fraction varies from 0.15 near the center-plane to about 0.02 near the free surface. The reason for the high values of f near the center-plane as compared to the free surface is because of a strongly triaxial stress field prevailing near the center-plane of the specimen which promotes rapid void growth as noted earlier.

In Fig. 15, the hydrostatic stress normalized by the initial matrix yield stress σ_0 is plotted against radial distance (normalized by the initial notch opening b_0) ahead of the tip at the point of incipient material failure. Results are presented from the 3-D simulation corresponding to three different planes through the specimen thickness, which are near the center-plane, quarter-plane, and free surface, in order to highlight also the thickness variations of the hydrostatic stress. Plane strain results at the point of incipient material damage are also included in the figure for comparison.

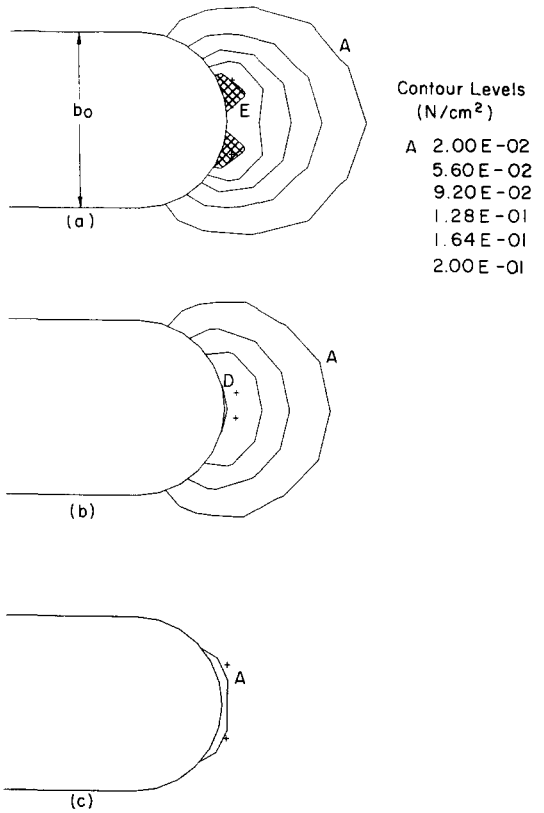

Fig. 13. Contours of f in three different planes through the specimen thickness: (a) $x_3/h = 0.057$, (b) $x_3/h = 0.282$, (c) $x_3/h = 0.485$.

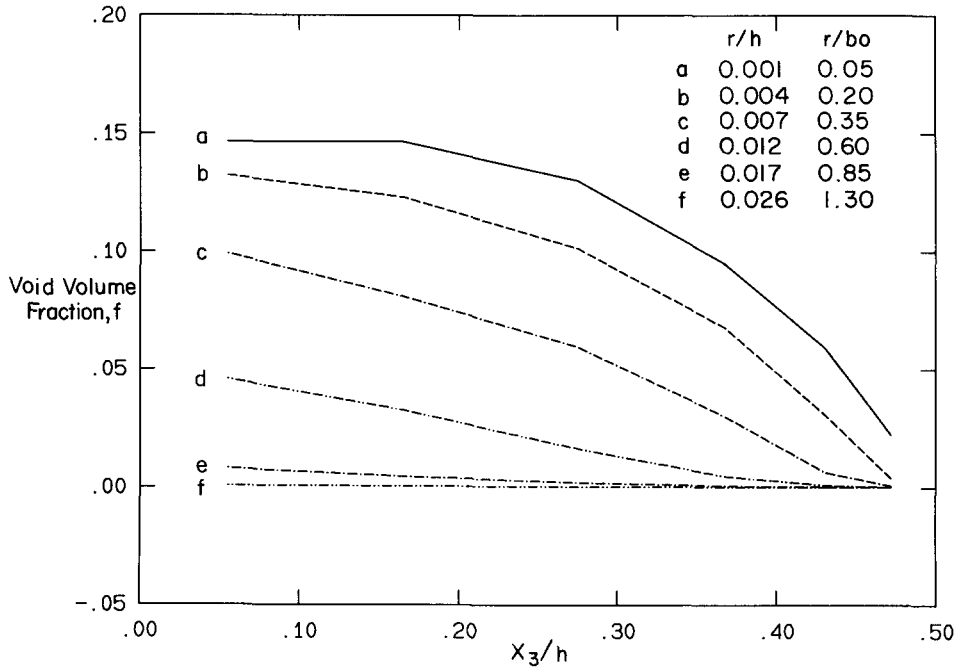

Fig. 14. Variation of the void volume fraction, f, through the thickness at different radial distances ahead of the notch tip.

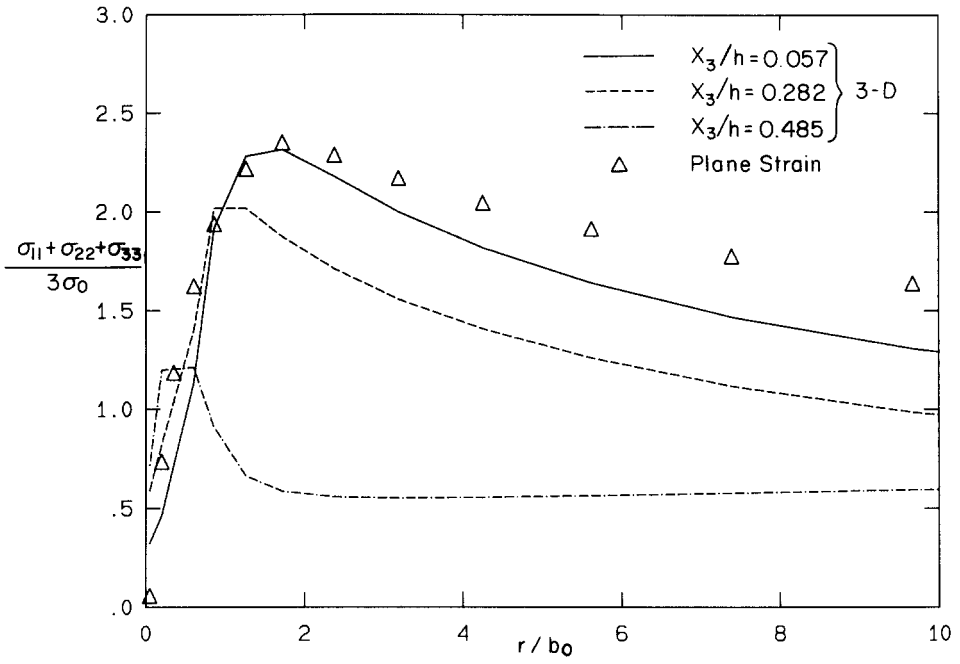

Fig. 15. Radial variation of normalized hydrostatic stress along three different planes through the specimen thickness. Comparison between 3-D and plane strain.

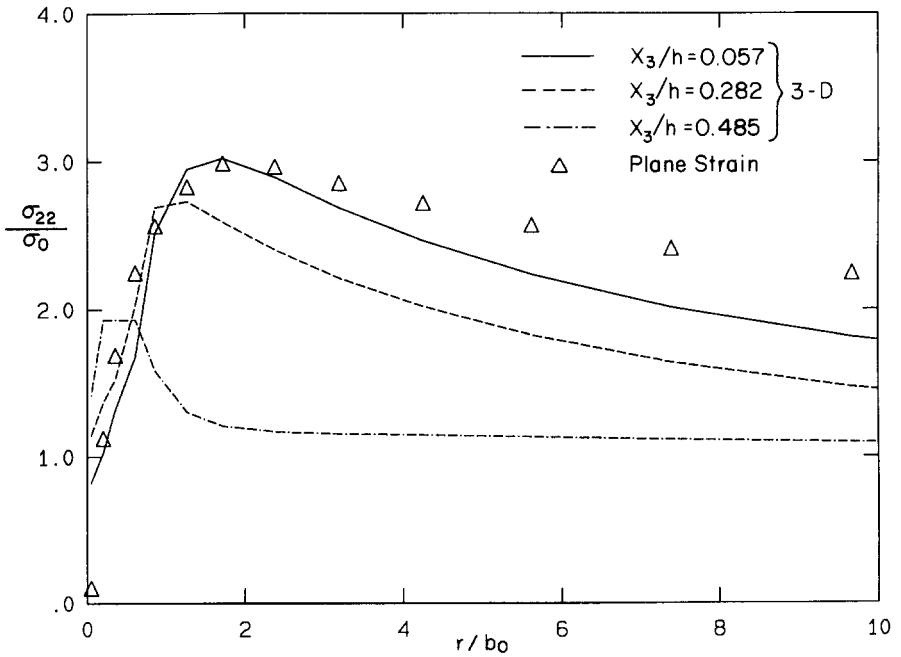

Fig. 16. Radial variation of σ_{22}/σ_0 along three different planes through the specimen thickness. Comparison between 3-D and plane strain.

It should be noted that the hydrostatic stress levels are highest near the center-plane and decrease as the free surface is approached (see also the colour band contours in Fig. 11). The peak value reached in the center-plane at around two notch openings ($2b_0$) ahead of the tip is $2.3\sigma_0$. This value is in reasonable agreement with the plane strain HRR field [28, 29] for low hardening materials. Also, the close comparison between 3-D center-plane and plane strain results should be noted.

The radial variation of the normalized opening stress, σ_{22}/σ_0, versus normalized distance ahead of the tip, r/b_0, is shown in Fig. 16 for the 3-D case along with the plane strain results. The trend is similar to Fig. 15 for the hydrostatic stress with the peak values being reached in the center-plane. The maximum value of σ_{22} in the center-plane is about $3\sigma_0$, again in good agreement with the plane strain HRR field [28, 29] for low hardening materials.

Appendix A

Experimental justification for the choice of values for f_F, f_n, s_n and ε_n

Qualitative and quantitative micromechanical information provided by Cox and Low [1] for the same heat treatment of high purity AISI 4340 steel as used by Zehnder and Rosakis [8] will be used here to provide estimates for some of the constitutive parameters of the continuum damage model used in the investigation.

An average estimate of f_F, the void volume fraction at failure, is obtained by referring to Table III and to Figs. 15 and 16 of [1]. Figures 15 and 16 show the coalescence of voids whose average radius ρ_F (just before failure) is 15–25 μm. In addition, Table III provides an average estimate of N_v, the number of void nucleation sites per unit volume, as approximately 7×10^6 inclusions /cm^3. Assuming that the resulting voids are spherical, one obtains an average value of $f_N = 4/3N_v\pi\rho_F^3 \sim 0.23$ which is close to the value of 0.25 used here and which is also suggested by Anderson [18] on the basis of a numerical investigation.

The choice of $f_n = 0.04$, $s_n = 0.1$, and $\varepsilon_n = 0.3$ is indirectly justified by the following calculation. The constitutive equations (2.1) – (2.12) (also see Appendix B) are specialized to **uniaxial tension** and are integrated numerically to obtain $f = \hat{f}(\varepsilon)$, the relation between the void volume fraction and the uniaxial strain ε. By assuming spherical void geometries, the average void radius ρ_A can also be obtained as a function of ε. ($\rho_A(\varepsilon) = (3\hat{f}(\varepsilon)/4N_V)^{1/3}$ and N_v is the number of void nucleation sites per unit volume.) This function is shown in Fig. 1A together with the measurements reported by Cox and Low [1] obtained from experiments in **uniaxial tension** of high purity AISI 4340 steel. The experimental points are taken from Fig. 13 of [1] and correspond to their unnotched (smooth) tension test specimens. For this specimen deformation, a very good agreement between experiment and theory is obtained for the above choice of f_n, s_n, and ε_n and for the average value of N_v reported in Table III of [1].

Although such a comparison is naturally not enough to determine the values of the triplet f_n, s_n and ε_n uniquely, its success over a wide range of strains suggests that the values used here are reasonable for the material to be modeled. However, it should be noted that the unique determination of f_n, s_n and ε_n could not have been achieved if experimental evidence of void growth under other simple deformation regimes (e.g. simple shear) were also available.

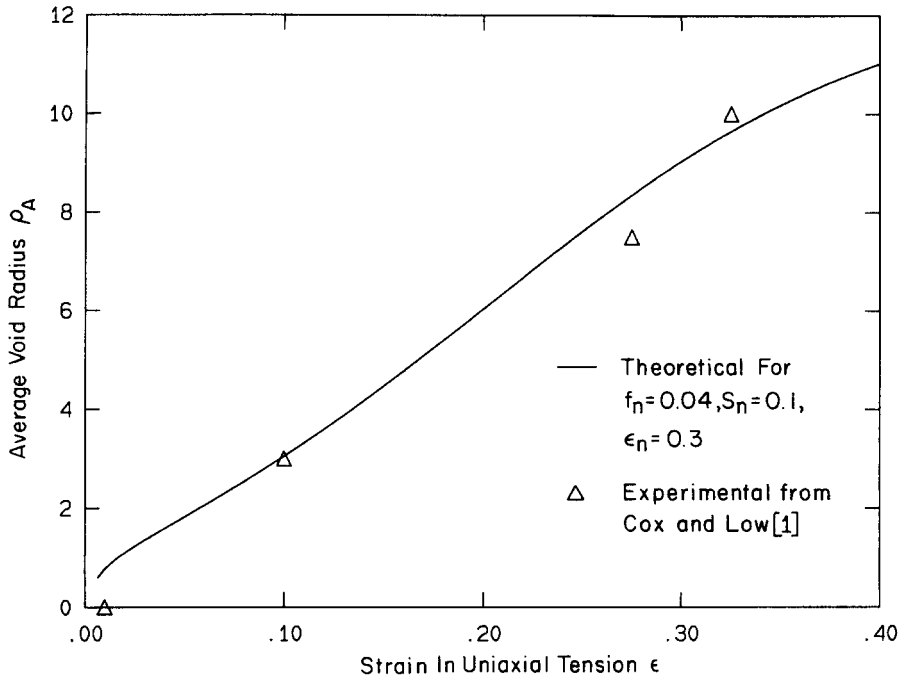

Fig. A1. Variation of average void radius with strain in uniaxial tension. Solid line is obtained from void nucleation and growth model with $f_n = 0.04$ $s_n = 0.1$ and $\varepsilon_n = 0.3$. The discrete points are experimental data from Fig. 13 of [1].

Appendix B

Explicit integration of constitutive equations

The constitutive equations for an elastic-plastic material obeying an incremental theory are summarized below. The infinitesimal strain rate tensor $\dot{\varepsilon}$ is decomposed into elastic and plastic parts:

$$\dot{\varepsilon} = \dot{\varepsilon}^e + \dot{\varepsilon}^P. \tag{B.1}$$

The stress rate tensor is related to the elastic strain rate tensor through a constant, isotropic, positive definite elasticity tensor C as:

$$\dot{\sigma} = C{:}\dot{\varepsilon}^e. \tag{B.2}$$

The yield condition is written as:

$$\Phi(\sigma, x) = 0, \tag{B.3}$$

where $x_\alpha (\alpha = 1, 2, \ldots, n)$ represent a set of plastic history variables. The flow rule is described by,

$$\dot{\varepsilon}^P = \dot{\lambda} r(\sigma, x), \tag{B.4}$$

where $\dot{\lambda} \geqslant 0$ is a plastic parameter and $\boldsymbol{r}(\boldsymbol{\sigma}, \boldsymbol{x})$ is the flow direction tensor. The evolution laws for the plastic variables are given by,

$$\dot{\boldsymbol{x}} = \dot{\lambda}\boldsymbol{h}(\boldsymbol{\sigma}, \boldsymbol{x}), \tag{B.5}$$

where $h_\alpha(\boldsymbol{\sigma}, \boldsymbol{x})$ represent plastic moduli.

The loading/unloading conditions are described by the following equations (see Section 2):

$$\left.\begin{aligned} \Phi(\boldsymbol{\sigma}, \boldsymbol{x}) &\leqslant 0 \\ \dot{\lambda} &\geqslant 0 \\ \Phi\dot{\lambda} &= 0 \end{aligned}\right\}. \tag{B.6}$$

Finally, the normals to the yield surface in stress space and plastic variable space are denoted by $\boldsymbol{v}$, and $\boldsymbol{\xi}$, so that,

$$\left.\begin{aligned} \boldsymbol{v}(\boldsymbol{\sigma}, \boldsymbol{x}) &= \nabla_\sigma \Phi(\boldsymbol{\sigma}, \boldsymbol{x}) \\ \boldsymbol{\xi}(\boldsymbol{\sigma}, \boldsymbol{x}) &= \frac{\partial \Phi}{\partial \boldsymbol{x}}(\boldsymbol{\sigma}, \boldsymbol{x}) \end{aligned}\right\}. \tag{B.7}$$

By using consistency $(B.6)_3$ along with (B.1)–(B.5) the plastic parameter $\dot{\lambda}$ may be obtained as:

$$\dot{\lambda} = \frac{\boldsymbol{v}:\boldsymbol{C}:\dot{\boldsymbol{\varepsilon}}}{(\boldsymbol{v}:\boldsymbol{C}:\boldsymbol{r} - \boldsymbol{\xi}\cdot\boldsymbol{h})}. \tag{B.8}$$

For the Gurson yield function Φ given by (2.1), there are two plastic variables $x_1 = \sigma_m$ and $x_2 = f$. The normal to the yield function in stress space v_{ij} and plastic variable space ξ_1 and ξ_2 is given by,

$$\left.\begin{aligned} v_{ij} &= \frac{\partial \Phi}{\partial \sigma_{ij}} = \frac{2}{\sigma_m}\left(\frac{3S_{ij}}{2\sigma_m} + \beta S_{ij}\right) \\ \xi_1 &= \frac{\partial \Phi}{\partial \sigma_m} = -\frac{2}{\sigma_m}\left(\omega + \beta\frac{\sigma_{kk}}{\sigma_m}\right) \\ \xi_2 &= \frac{\partial \Phi}{\partial f} = 2q_1\left(\cosh\left(\frac{\sigma_{kk}}{2\sigma_m}\right) - f^* q_1\right)\frac{\partial f^*}{\partial f} \end{aligned}\right\}. \tag{B.9}$$

The variables β and ω that occur in the above equations are defined as follows:

$$\left.\begin{aligned} \beta &= \frac{f^* q_1}{2}\sinh\left(\frac{\sigma_{kk}}{2\sigma_m}\right) \\ \omega &= \frac{3S_{ij}S_{ij}}{2\sigma_m^2} \end{aligned}\right\}. \tag{B.10}$$

The plastic flow direction tensor $r_{ij} = v_{ij}$ and the plastic moduli are given by:

$$\left.\begin{aligned} h_1 &= \frac{2H_m}{(1-f)\sigma_m}\left(\omega + \beta\frac{\sigma_{kk}}{\sigma_m}\right) \\ h_2 &= \frac{6\beta(1-f)}{\sigma_m} + \frac{A}{H_m}h_1 \end{aligned}\right\}. \tag{B.11}$$

Here,

$$H_m = \frac{d\sigma_m}{d\varepsilon_m^P} = \frac{1}{E_t} - \frac{1}{E} \tag{B.12}$$

represents the hardening modulus of the tensile flow stress-plastic strain curve of the matrix material.

The following Box summarizes the stress update algorithm. This is a modified version of the explicit integration procedure with subincrementation employed by Narasimhan and Rosakis [21]. The task here is to compute the state variables $\boldsymbol{\varepsilon}_{n+1}$, $\boldsymbol{\varepsilon}_{n+1}^P$, $\boldsymbol{\sigma}_{n+1}$, and $\boldsymbol{x}_{x+1}$ corresponding to the load step $n+1$, given the values of these variables $\boldsymbol{\varepsilon}_n$, $\boldsymbol{\varepsilon}_n^P$, $\boldsymbol{\sigma}_n$, and $\boldsymbol{x}_n$ at the load step n along with the displacement increment $\boldsymbol{u}$.

Box 1: Stress update algorithm

1. Perform geometric update:

   $\boldsymbol{\varepsilon}_{n+1} = \boldsymbol{\varepsilon}_n + \frac{1}{2}(\boldsymbol{\nabla u} + \boldsymbol{\nabla}^T\boldsymbol{u})$

   $\Delta\boldsymbol{\varepsilon}_{n+1} = \boldsymbol{\varepsilon}_{n+1} - \boldsymbol{\varepsilon}_n$.

2. Obtain elastic predictor:

   $\boldsymbol{\varepsilon}_{n+1}^{P(E)} = \boldsymbol{\varepsilon}_n^P$; $\boldsymbol{x}_{n+1}^{(E)} = \boldsymbol{x}_n$;

   $\boldsymbol{\sigma}_{n+1}^{(E)} = \boldsymbol{\sigma}_n + \boldsymbol{C}:\Delta\boldsymbol{\varepsilon}_{n+1}$.

3. Check for yielding:

   $\Phi_{n+1}^{(E)} = \Phi(\boldsymbol{\sigma}_{n+1}^{(E)}, \boldsymbol{x}_{n+1}^{(E)}) \leqslant 0$?

   Yes: $\boldsymbol{\varepsilon}_{n+1}^P = \boldsymbol{\varepsilon}_{n+1}^{P(E)}$; $\boldsymbol{\sigma}_{n+1} = \boldsymbol{\sigma}_{n+1}^{(E)}$ $\boldsymbol{x}_{n+1} = \boldsymbol{x}_{n+1}^{(E)}$:Exit.
   No: Go to Step 4.

4. Compute contact stress state:

   $\Phi_n = \Phi(\boldsymbol{\sigma}_n, \boldsymbol{x}_n) = 0$?

   Yes: $\rho = 0$.

No: Calculate factor $\rho(0 < \rho < 1)$ such that:

$$\Phi(\boldsymbol{\sigma}_n + \rho \boldsymbol{C}:\Delta\boldsymbol{\varepsilon}_{n+1}) = 0.$$

A Newton-Raphson iteration scheme is used to compute ρ from the above non-linear equation. Calculate the following:

$$\boldsymbol{\sigma}_{n+1}^{(0)} = \boldsymbol{\sigma}_n + \rho \boldsymbol{C}:\Delta\boldsymbol{\varepsilon}_{n+1},$$

$$\Delta\boldsymbol{\varepsilon}_{n+1}^{m} = (1 - \rho)\Delta\boldsymbol{\varepsilon}_{n+1}/m,$$

$$\boldsymbol{\varepsilon}_{n+1}^{P(0)} = \boldsymbol{\varepsilon}_n^P \text{ and } \boldsymbol{x}_{n+1}^{(0)} = \boldsymbol{x}_n.$$

Here m is the number of subincrements. Set $i = 0$.

5. Compute:

$$\boldsymbol{v}_{n+1}^{(i)} = \boldsymbol{v}(\boldsymbol{\sigma}_{n+1}^{(i)}, \boldsymbol{x}_{n+1}^{(i)}); \quad \boldsymbol{r}_{n+1}^{(i)} = \boldsymbol{r}(\boldsymbol{\sigma}_{n+1}^{(i)}, \boldsymbol{x}_{n+1}^{(i)}),$$

$$\xi_{n+1}^{(i)} = \xi(\boldsymbol{\sigma}_{n+1}^{(i)}, \boldsymbol{x}_{n+1}^{(i)}); \quad \boldsymbol{h}_{n+1}^{(i)} = \boldsymbol{h}(\boldsymbol{\sigma}_{n+1}^{(i)}, \boldsymbol{x}_{n+1}^{(i)}),$$

$$\Delta\lambda = \frac{\boldsymbol{v}_{n+1}^{(i)}:\boldsymbol{C}:\Delta\boldsymbol{\varepsilon}_{n+1}^{m}}{(\boldsymbol{v}_{n+1}^{(i)}:\boldsymbol{C}:\boldsymbol{r}_{n+1}^{(i)} - \xi_{n+1}^{(i)} \cdot \boldsymbol{h}_{n+1}^{(i)}}.$$

6. Obtain state variables for the $(i + 1)th$ subincrement:

$$\boldsymbol{\varepsilon}_{n+1}^{P(i+1)} = \boldsymbol{\varepsilon}_{n+1}^{P(i)} + \Delta\lambda \boldsymbol{r}_{n+1}^{(i)},$$

$$\boldsymbol{\sigma}_{n+1}^{(i+1)} = \boldsymbol{\sigma}_{n+1}^{(i)} + \boldsymbol{C}:(\Delta\boldsymbol{\varepsilon}_{n+1}^{m} - \Delta\lambda \boldsymbol{r}_{n+1}^{(i)}),$$

$$\boldsymbol{x}_{n+1}^{(i+1)} = \boldsymbol{x}^{(i)} + \Delta\lambda \boldsymbol{h}_{n+1}^{(i)}.$$

7. Return stress state to updated yield surface. Compute factor γ (by Newton-Raphson method) such that:

$$\Phi(\gamma\boldsymbol{\sigma}^{(i+1)}, \boldsymbol{x}^{(i+1)}) = 0.$$

$$\boldsymbol{\sigma}_{n+1}^{(i+1)} \leftarrow \gamma\boldsymbol{\sigma}_{n+1}^{(i+1)}.$$

8. $i \leftarrow (i + 1)$. If $i < m$ go to step 5.

9. The final updated state variables are:

$$\boldsymbol{\sigma}_{n+1} = \boldsymbol{\sigma}_{n+1}^{(i)}; \quad \boldsymbol{x}_{n+1} = \boldsymbol{x}_{n+1}^{(i)}; \quad \boldsymbol{\varepsilon}_{n+1}^{P} = \boldsymbol{\varepsilon}_{n+1}^{P(i)}.$$

The above algorithm was tested by performing a number of simple tests such as uniaxial tension, hydrostatic tension and simple shear. The results from these studies were compared with exact integration of the rate equations for the corresponding cases and were found to be in very good agreement.

Acknowledgements

Support of ONR through Contract N00014-85-K-0596 and of NSF through the Presidential Young Investigator Award (Grant MSM-84-51204) to the second author is gratefully acknowledged. Also, Brian Moran is grateful for the support of an IBM Research Fellowship at Caltech in 1987/88.

References

1. T.B. Cox and J.R. Low, *Metallurgical Transactions* 5 (1974) 1457–1470.
2. F.A. McClintock, *Journal of Applied Mechanics* 35 (1968) 363–371.
3. J.R. Rice and D.M. Tracey, *Journal of Mechanics and Physics of Solids* 17 (1969) 201–217.
4. H.C. Rogers, *Transactions of Metallurgical Society AIME* 218 (1960) 498–506.
5. V. Tvergaard, *International Journal of Fracture* 17 (1981) 389–407.
6. S.H. Goods and L.M. Brown, *Acta Metallurgica 27* (1979) 1–15.
7. L.M. Brown and J.D. Embury, in *The Microstructure and Design of Alloys*, Proceedings of the 3rd International Conference on the Strength of Metals and Alloys, Cambridge, England (1973).
8. A.T. Zehnder and A.J. Rosakis, *Journal of Applied Mechanics*, to appear.
9. R. Narasimhan and A.J. Rosakis, *Journal of Applied Mechanics*, to appear.
10. A.T. Zehnder, A.J. Rosakis and S. Krishnaswamy, *International Journal of Fracture* 43 (1990) 209–230.
11. A.L. Gurson, Transactions of the American Society of Mechanical Engineers, Series H, *Journal of Engineering Materials and Technology* 99 (1977) 2–15.
12. V. Tvergaard and A. Needleman, *Acta Metallurgica* 32 (1984) 157–169.
13. S. Aoki, K. Kishimoto, A. Takeya and M. Sakata, *International Journal of Fracture* 24 (1984) 267–278.
14. N. Aravas and R.M. McMeeking, *International Journal of Fracture* 29 (1985) 21–38.
15. A. Jagota, C.Y. Hui and P.R. Dawson, *International Journal of Fracture* 33 (1987) 111–124.
16. R. Becker, A. Needleman, S. Suresh, V. Tvergaard and A.K. Vasudevan, *Acta Metallurgica* 37 (1989) 99–120.
17. R. Becker, A. Needleman, O. Richmond and V. Tvergaard, *Journal of Mechanics and Physics of Solids* 36 (1988) 317–351.
18. H. Andersson, *Journal of Mechanics and Physics of Solids* 25 (1977) 217–233.
19. C.C. Chu and A. Needleman, Transactions of American Society of Mechanical Engineers, Series H, *Journal of Engineering Materials and Technology* 102 (1980) 249–256.
20. C.A. Berg, in *Inelastic Behavior of Solids*, M.F. Kanninen, W.F. Adler, A.R. Rosenfield and R.I. Jaffee (eds.), McGraw-Hill (1970) 171–209.
21. R. Narasimhan and A.J. Rosakis, *Journal of Mechanics and Physics of Solids* 36 (1988) 77–117.
22. H. Mathies and G. Strang, *International Journal for Numerical Methods in Engineering* 14 (1979) 1613–1626.
23. V. Tvergaard, *Journal of Mechanics and Physics of Solids* 30 (1982) 399–425.
24. B. Budiansky and J.R. Rice, *Journal of Applied Mechanics* 40 (1973) 201–203.
25. T. Nakamura, C.F. Shih and L.B. Freund, *ASTM STP 995*, to appear.
26. F.Z. Li, C.F. Shih and A. Needleman, *Engineering Fracture Mechanics* 21 (1985) 405–421.
27. C.F. Shih, B. Moran and T. Nakamura, *International Journal of Fracture* 30 (1986) 79–102.
28. J.W. Hutchnson, *Journal of Mechanics and Physics of Solids* 16 (1986) 337–347.
29. J.R. Rice and G.F. Rosengren, *Journal of Mechanics and Physics of Solids* 16 (1968) 1–12.
30. C.F. Shih, *Journal of Mechanics and Physics of Solids* 29 (1981) 305–326.
31. R. Narasimhan, A.J. Rosakis and J.F. Hall, *Journal of Applied Mechanics* 54 (1987) 838–845.
32. J.R. Rice, in *Mechanics and Mechanisms of Crack Growth*, M.J. May, (ed.), British Steel Corp. Physical Metallurgy Centre Publication, Sheffield, England (1975) 14–39.
33. B. Moran, R.J. Asaro and C.F. Shih, *Metallurgical Transactions A* 22A (1991) 161–170.